Supplementary Information

Redirecting Iodine Reduction Pathways by Decoupling Adsorption Energies for Long-Life Zn–I_2 batteries

Maoxin Chen[1,2,3,4,#], Huan Li[5,#], Hui Xu[1,#], Zhitan Wu[1,2,4], Jinxing Chen[4], Huihui Lin[4], Ao Du[1], Sundus Umer[1], Zihui Chen[1], Ning Yue[1], Zhijie Yan[1], Tianyu Yin[1], Nianjun Yang[6], Jiong Lu[4], Weichao Wang[5]*, Chunpeng Yang[1,3]*, Quan-Hong Yang[1,2,3]*

[1]Nanoyang Group, Tianjin Key Laboratory of Advanced Carbon and Electrochemical Energy Storage, School of Chemical Engineering and Technology, and Collaborative Innovation Center of Chemical Science and Engineering (Tianjin), Tianjin University, Tianjin 300072, China

[2]Joint School of National University of Singapore and Tianjin University, International Campus of Tianjin University, Binhai New City, Fuzhou 350207, China

[3]Haihe Laboratory of Sustainable Chemical Transformations, Tianjin 300192, China

[4]Department of Chemistry, National University of Singapore, 3 Science Drive 3, Singapore 117543, Singapore

[5]College of Electronic Information and Optical Engineering, Nankai University, Tianjin 300071, China

[6]Department of Chemistry, Hasselt University, 3590 Diepenbeek, Belgium

[#]These authors contributed equally to this work.

*E-mail: weichaowang@nankai.edu.cn; cpyang@tju.edu.cn; qhyangcn@tju.edu.cn

Methods

Chemicals

All chemicals were commercially available and used without further purification. Cobalt nitrate hexahydrate ($Co(NO_3)_2·6H_2O$, 99.0%), iron nitrate hexahydrate ($Fe(NO_3)_2·6H_2O$, 98.5%), nickel nitrate hexahydrate ($Ni(NO_3)_2·6H_2O$, 99.0%), and copper nitrate trihydrate ($Cu(NO_3)_2·3H_2O$, 99.0%), 2-methylimidazole (2-MI, 99.0%), Iodine (I_2, ≥99.99%) and polytetrafluoroethylene aqueous dispersion (PTFE, 60 wt.% solid content) were all obtained from Aladdin Chemistry Co., Ltd. (Shanghai, China). Zinc foils (100μm), Ketjen black (KB), carbon cloth (W1S1010), and glass fiber (GF/A, Whatman) were supplied by Canrd New Energy Technology Co., Ltd.

Preparation for ACCs

The ACCs were synthesized through a solvothermal method followed by high-temperature calcination. A solution containing 2.3 mmol of $Co(NO_3)_2·6H_2O$ and 2.5 mmol of $Zn(NO_3)_2·6H_2O$ was added to 50 mL of methanol and ultrasonicated for 15 minutes. Separately, 10 mol of 2-methylimidazole was dissolved in another 50 mL of methanol and ultrasonicated for 15 minutes. The metal salt solution was then slowly added to the ligand solution, followed by an additional 15 minutes of ultrasonic mixing. The resulting mixture was vigorously stirred for 12 hours under magnetic agitation. After the reaction, the product was collected by centrifugation at 8000 rpm for 5 minutes, washed with methanol, and centrifuged three more times until the supernatant became colorless. The final solid was dried in an oven at 80 °C. The dried precursor was then subjected to pyrolysis in a tube furnace under an argon atmosphere. The temperature was ramped at a rate of 5 °C/min to 900 °C and held for 2 hours to obtain the

Zn_1Co ACCs. Using the same procedure, $Fe(NO_3)_3 \cdot 6H_2O$, $Ni(NO_3)_2 \cdot 6H_2O$, or $Cu(NO_3)_2 \cdot 3H_2O$ can be used in place of $Co(NO_3)_2 \cdot 6H_2O$ to prepare different ACCs, respectively.

Preparation for ACCs/I_2 electrodes

The ACCs/I_2 cathode was prepared using a melt-diffusion method. In a typical process, activated carbon and iodine (I_2) were mixed in a mass ratio of 1:1 and sealed in a glass bottle. The sealed mixture was then heated at 100°C for 6 hours to allow the iodine to diffuse into the carbon framework. After cooling to room temperature, the iodine-loaded carbon composite was mixed with ACCs, KB, and PTFE binder in a mass ratio of 5:2:2:1. For the blank sample, the iodine-loaded carbon composite, KB, and PTFE binder were mixed in a ratio of 5:4:1, excluding ACCs. The resulting mixture was ground into a homogeneous paste and then repeatedly rolled using a roller press to form a flexible electrode, which was then compressed onto a carbon cloth. The prepared electrodes were cut into 10 mm pieces and dried at room temperature for 6 hours to remove any residual solvents. The areal mass loading of iodine in the cathodes, including all electrochemical tests and spectroscopy analysis, was controlled within the range of 6.5–10 mg cm^{-2}. For the soft pouch cell, the electrode preparation method was similar, except the electrodes were pressed onto both sides of a titanium mesh, with mass loading of 30 mg cm^{-2} and an area of 5×5 cm^2.

Characterization

Scanning electron microscope (SEM) was performed on a Regulus 8100 (Hitachi, Japan) with an accelerating voltage of 3.0 kV. Transmission electron microscopy (TEM) was performed on a JEM-F200 (JEOL, Japan) with an accelerating voltage of 200 kV. The X-ray diffraction (XRD) patterns were collected on a Bruker D-8 (Cu Kα radiation, λ=0.154056 nm) at room

temperature. X-ray photoelectron spectroscopy (XPS) measurement was carried out on a Thermo Fisher Scientific ESCALAB 250Xi system with an Al Kα X-ray source (1486.6 eV) operating at 15 kV. The binding energies were calibrated using the C 1s peak at 284.8 eV as a reference. The nitrogen adsorption-desorption isotherms were obtained using a BELSORP-max II (BEL Inc., Japan) at 77K. The specific surface area was calculated using the Brunauer-Emmett-Teller (BET) theory. The pore size distribution was analyzed based on density functional theory (DFT) methods. In situ Raman spectra were recorded on MicroRaman system (LabRAM HR spectrometer, Horiba) with the laser of 532 nm, by monitoring the cathode surface through the quartz window of a custom two-electrode cell (IVIUM, Netherlands) during galvanostatic charge-discharge cycles. In situ ultraviolet–visible (UV–vis) spectra were conducted using an Evolution 220 (Thermo Fisher Scientific, USA). A 1 cm path length quartz cuvette served as the electrochemical cell, with the cathode and anode secured on opposite sides to ensure absorbance values within the optimal linear range.

Electrochemical measurements

The cyclic voltammetry (CV), and electrochemical impedance spectroscopy (EIS) tests were conducted at room temperature using a Princeton workstation (PMC-200, USA). EIS tests were performed in frequency ranging from 100 kHz to 0.01 Hz at open circuit potential by applying a potential amplitude of 5 mV. Galvanostatic charge/discharge tests were conducted with a LAND (CT3002A) battery tester and a Neware battery testing system (MIHW-200-160CH, Shenzhen, China). The cathode and polished Zn foil (100 μm) are utilized to assemble the coin cells (CR-2032). The electrolyte used was a 2M $ZnSO_4$ aqueous solution, with a volume of 80 μL per 2 mg cm^{-2} of cathode mass loading, and this ratio was scaled accordingly for different

loadings. Whatman glass fiber membrane was used as a separator. Galvanostatic cycling tests were conducted at a potential range of 0.5–1.6 V (vs. Zn^{2+}/Zn) based on the Land CT3002A system and Neware (MIHW-200-160CH) battery testing system. The RDE tests were conducted using a glassy carbon disk electrode coated with catalyst ink (2.5 mg catalyst dispersed in 980 μL isopropanol and 20 μL 5 wt% Nafion solution, 10 μL drop-cast), with a Pt wire as the counter electrode and Ag/AgCl as the reference electrode. The electrolyte consisted of 0.5 mM I_2 + 0.25 mM ZnI_2 aqueous solution, and LSV was performed in the potential range of 0.5 V to –1.25 V at a scan rate of 1 mV s^{-1}.

Computational Methods

All density functional theory (DFT) calculations were carried out using the Vienna Ab initio Simulation Package (VASP)[1]. The generalized gradient approximation (GGA) with the Perdew–Burke–Ernzerhof (PBE) functional was applied to describe the electronic exchange-correlation interactions, and the projector augmented wave (PAW) method was employed to treat the electron–ion interactions[2-5]. Graphene-based Zn SACs were modeled using a p (5 × 5) supercell with a lattice constant of 12.34 Å, constructed according to the $P6_3/mmc$ space group. Zn_1M ACCs were constructed using a larger p (10 × 5) supercell with lattice constants of 24.68 × 12.34 Å. In both models, selected carbon atoms were removed and substituted with metal centers coordinated by pyridinic nitrogen atoms. A vacuum slab of 15 Å was introduced along the z-direction to eliminate spurious interactions between periodic images. A plane-wave energy cutoff of 400 eV was used, based on convergence testing. The electronic self-consistent field (SCF) convergence criterion was set to 10^{-5} eV, and structural optimization was performed until the maximum residual force on each atom was below 0.04 eV/Å. All calculations were

spin polarized. Long-range dispersion interactions were corrected using Grimme's DFT-D3 method.

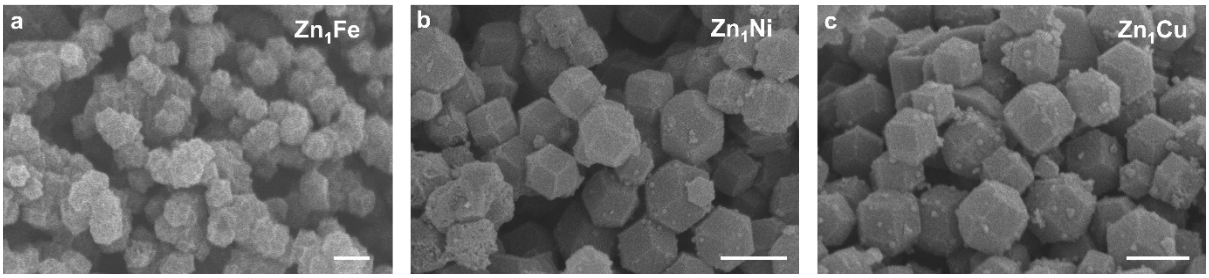

Fig. S1. (a–c) Scanning electron microscopy (SEM) images of (a) Zn_1Fe ACCs; (b) Zn_1Ni ACCs; and (c) Zn_1Cu ACCs (scale bars: 500 nm).

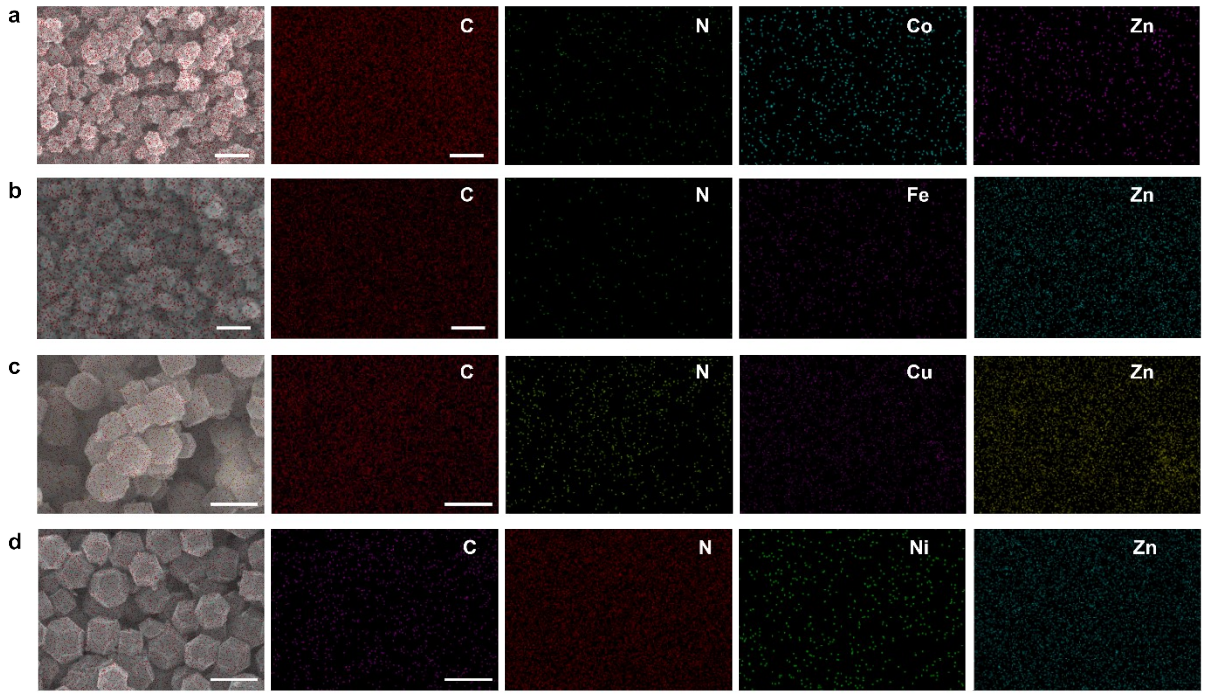

Fig. S2. (a–d) Elemental mapping of (a) Zn_1Co ACCs; (b) Zn_1Fe ACCs; (c) Zn_1Cu ACCs; and (d) Zn_1Ni ACCs (scale bars: 500 nm).

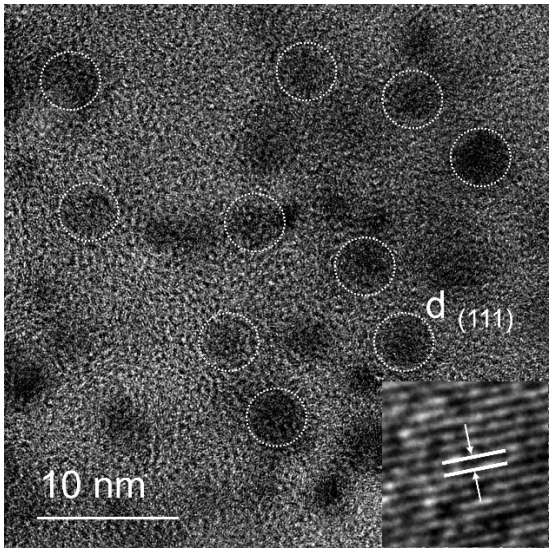

Fig. S3. HRTEM image of Zn_1Co ACCs. The inset shows a magnified view of the lattice fringes from the circled region, with the measured d-spacing labeled as $d_{(111)}$.

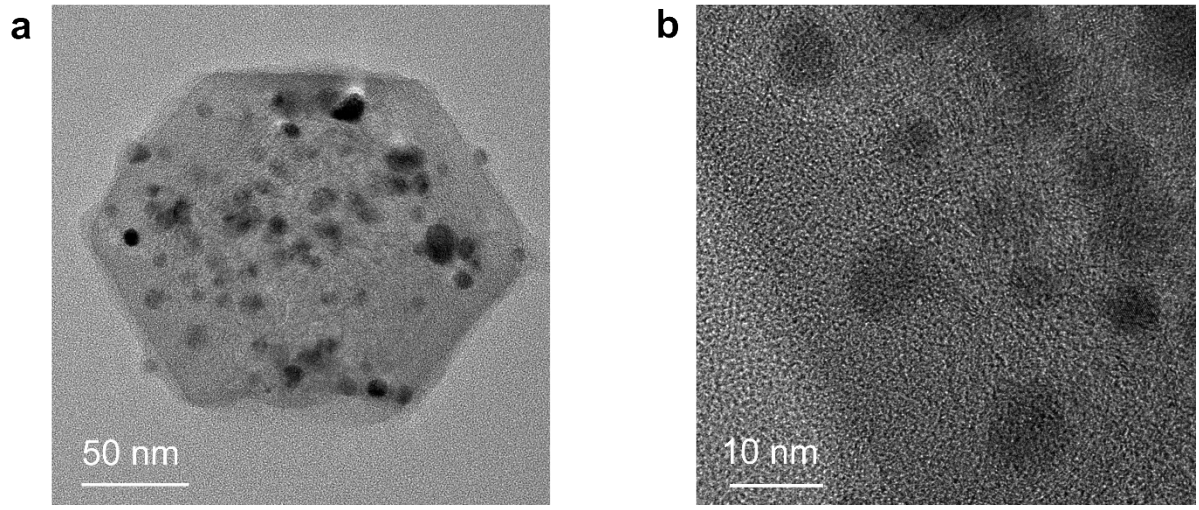

Fig. S4. (a) TEM image of Zn_1Fe ACCs confined within a hexagonal carbon framework. (b) High-resolution TEM image showing spherical nanoparticles with an average diameter of 10 nm.

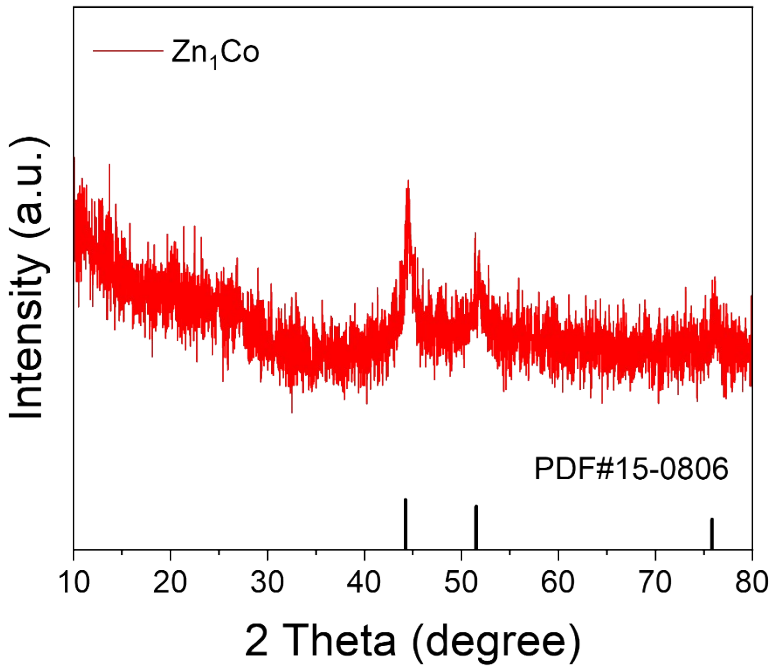

Fig. S5. XRD pattern for Zn_1Co ACCs.

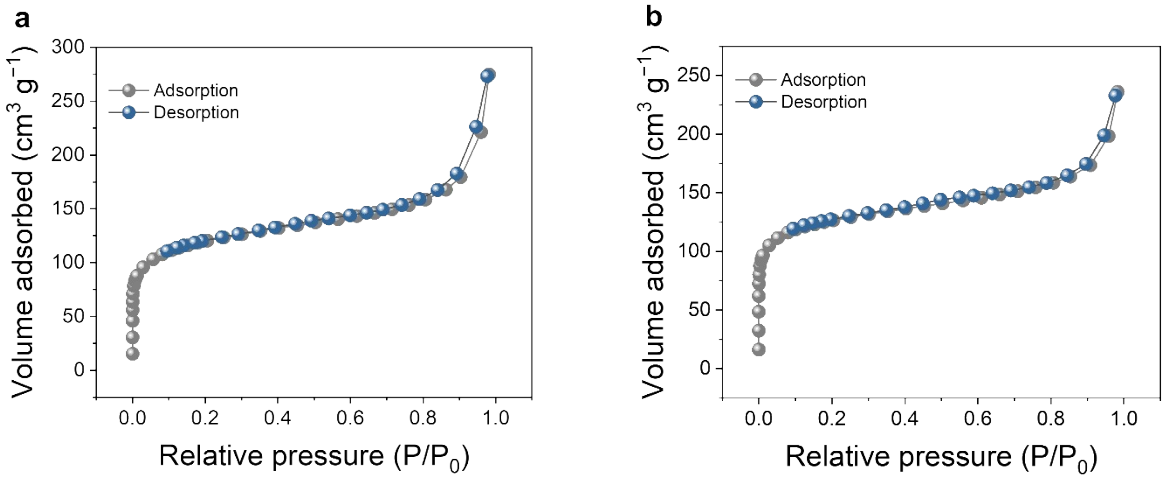

Fig. S6. Nitrogen adsorption-desorption isotherm for Zn_1Co and Zn_1Fe ACCs.

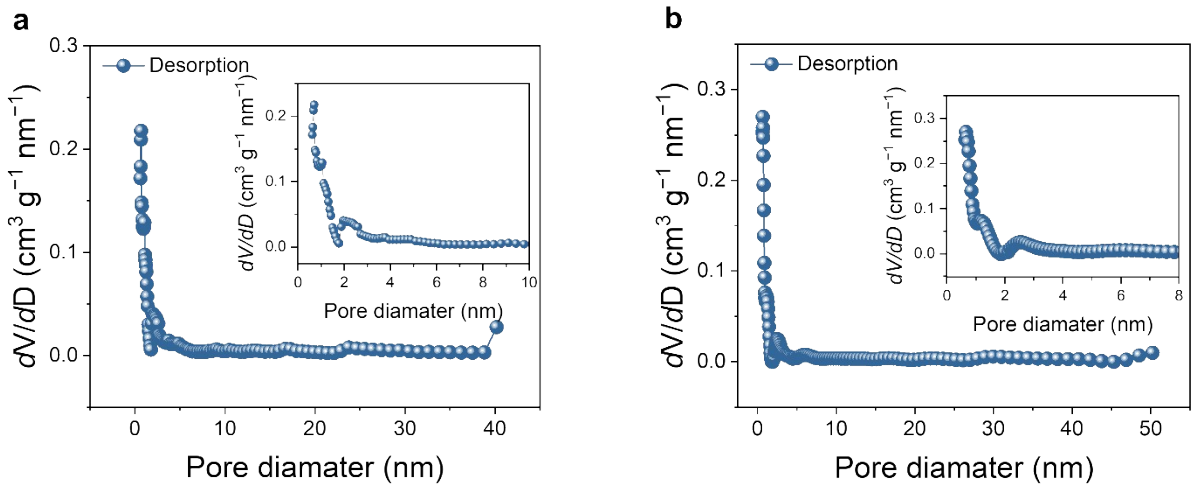

Fig. S7. Pore size distribution for Zn_1Co and Zn_1Fe ACCs.

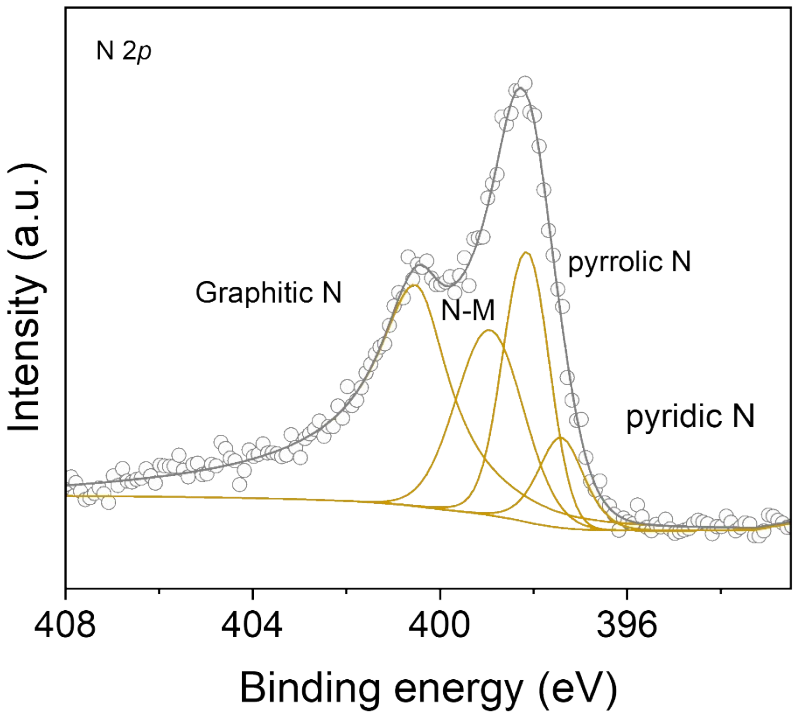

Fig. S8. High-resolution XPS spectra for N 2*p* for Zn_1Co ACCs.

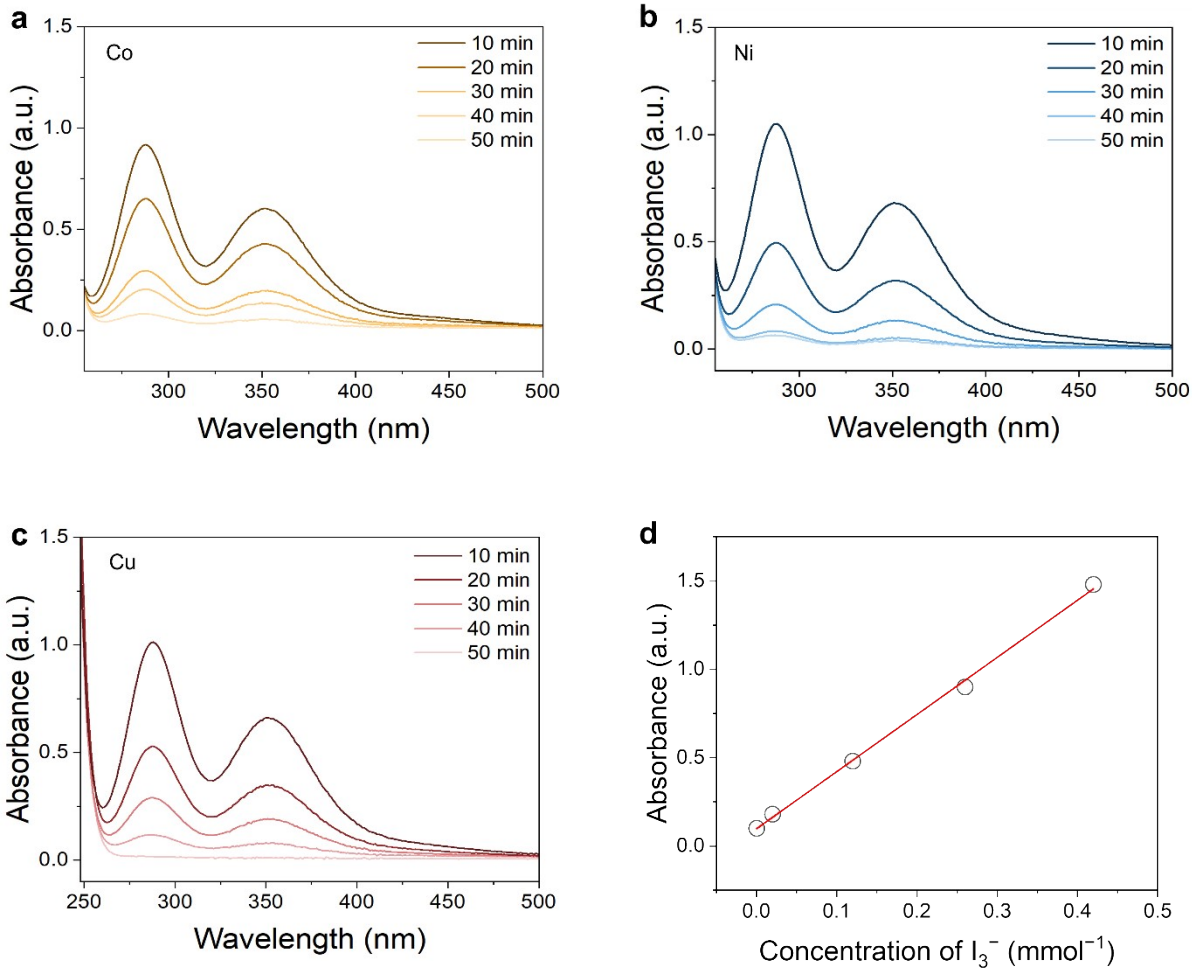

Fig. S9. (a–c) Time-dependent UV-vis absorption characteristics for Zn_1Co, Zn_1Ni, Zn_1Cu ACC, respectively; (d) Calibration curve for iodine quantification.

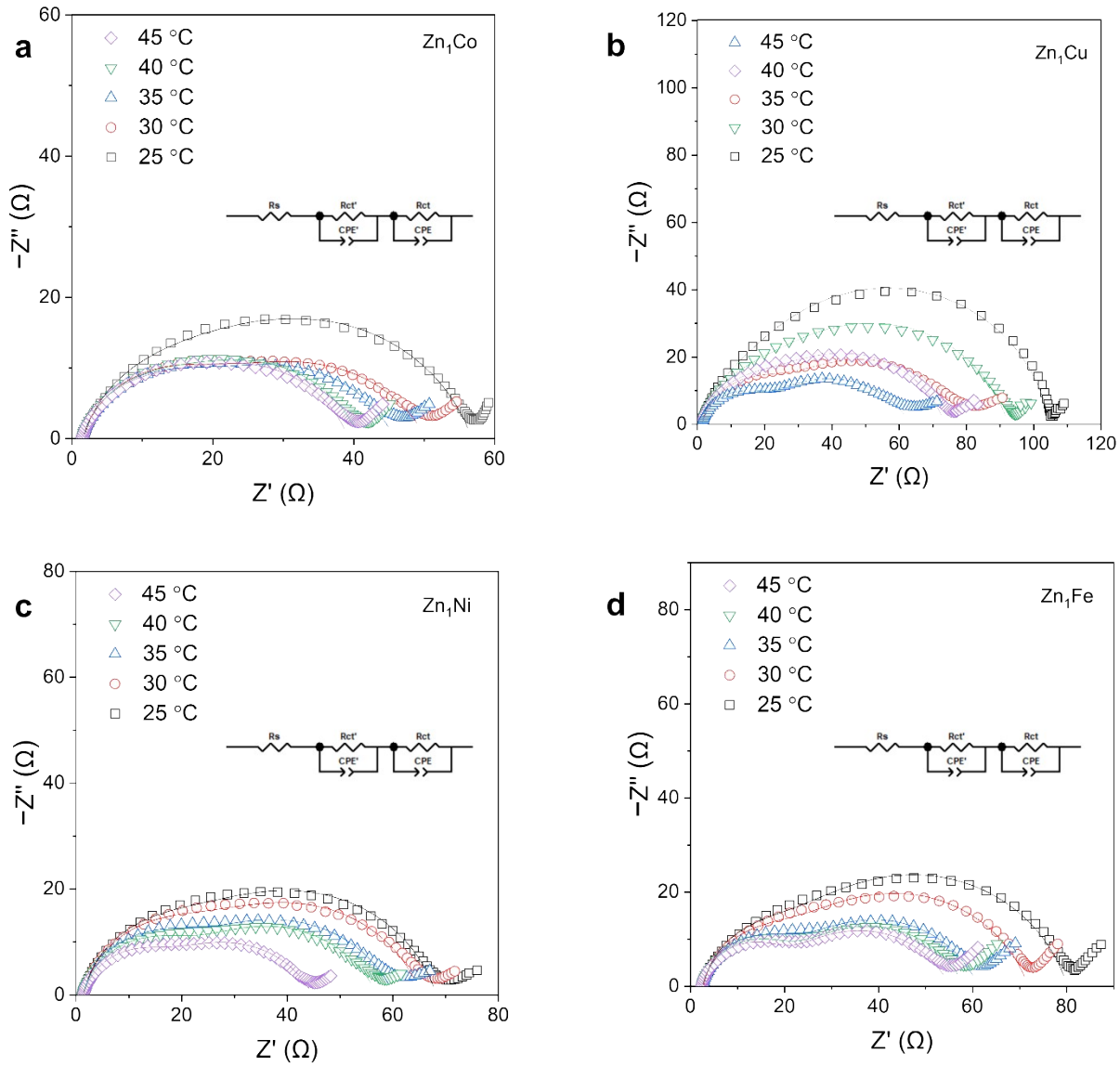

Fig. S10. Temperature-dependent EIS spectra for (a) Zn1Co, (b) Zn1Cu, (c) Zn1Ni, and (d) Zn1Fe ACCs electrodes.

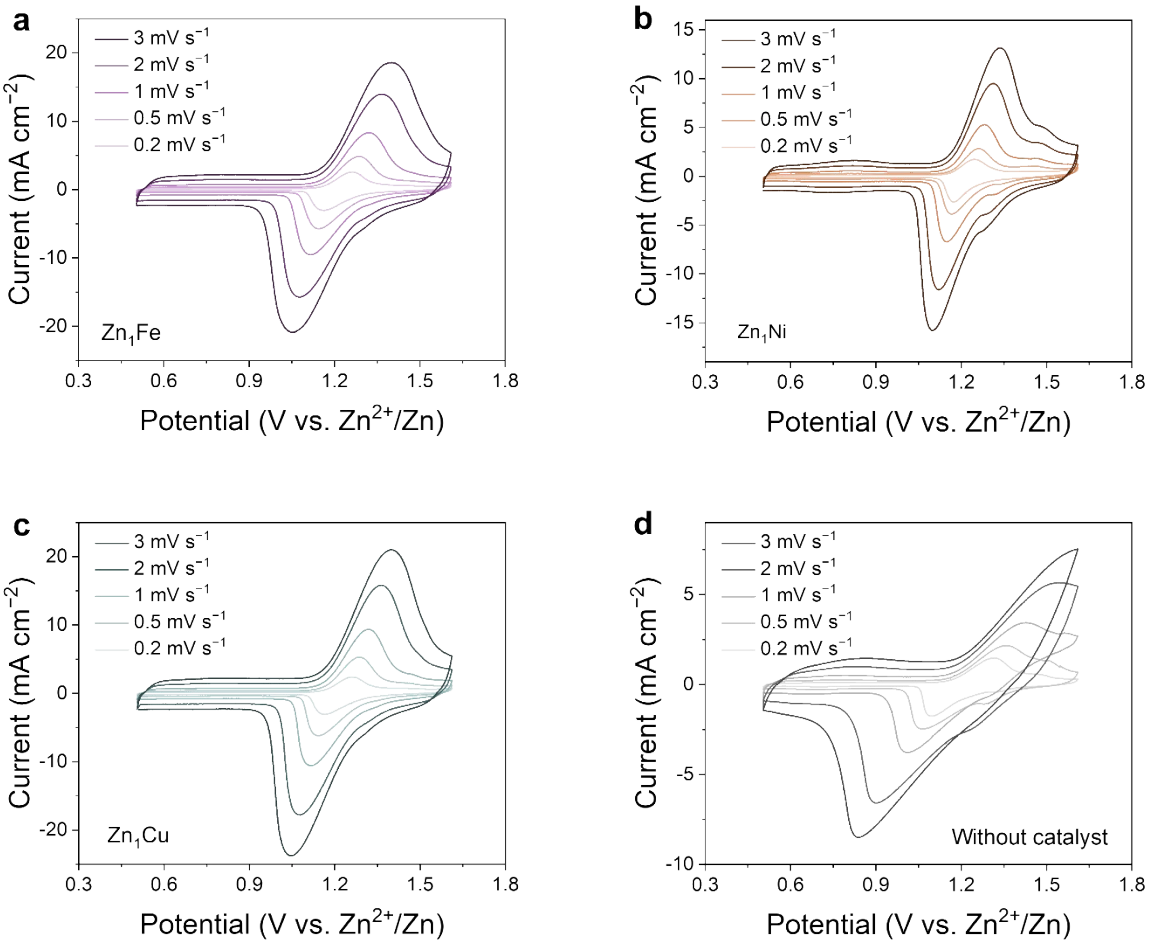

Fig. S11. CV curves for Zn_1Fe, Zn_1Ni, Zn_1Cu ACCs and catalyst-free system at scan rates from 0.2 to 3 mV s^{-1}.

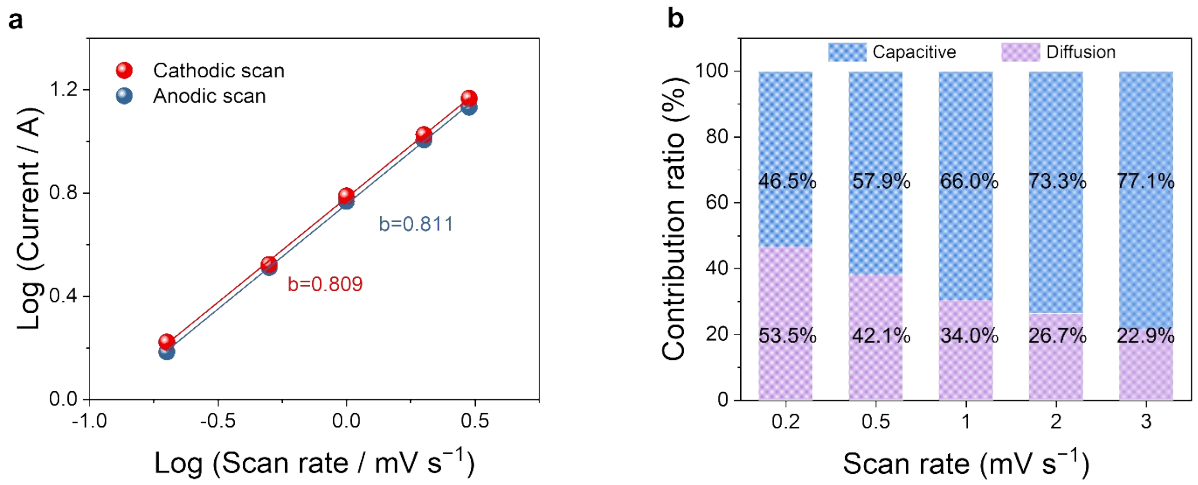

Fig. S12. (a) Logarithmic current vs. logarithmic scan rate plots for cathodic (purple spheres) and anodic (blue spheres) scans in CV; (b) The contribution ratios of capacitive (blue bars) and diffusion-controlled (pink bars) processes for Zn_1Co ACCs, measured at varying scan rates from 0.2 to 3 mV s^{-1}.

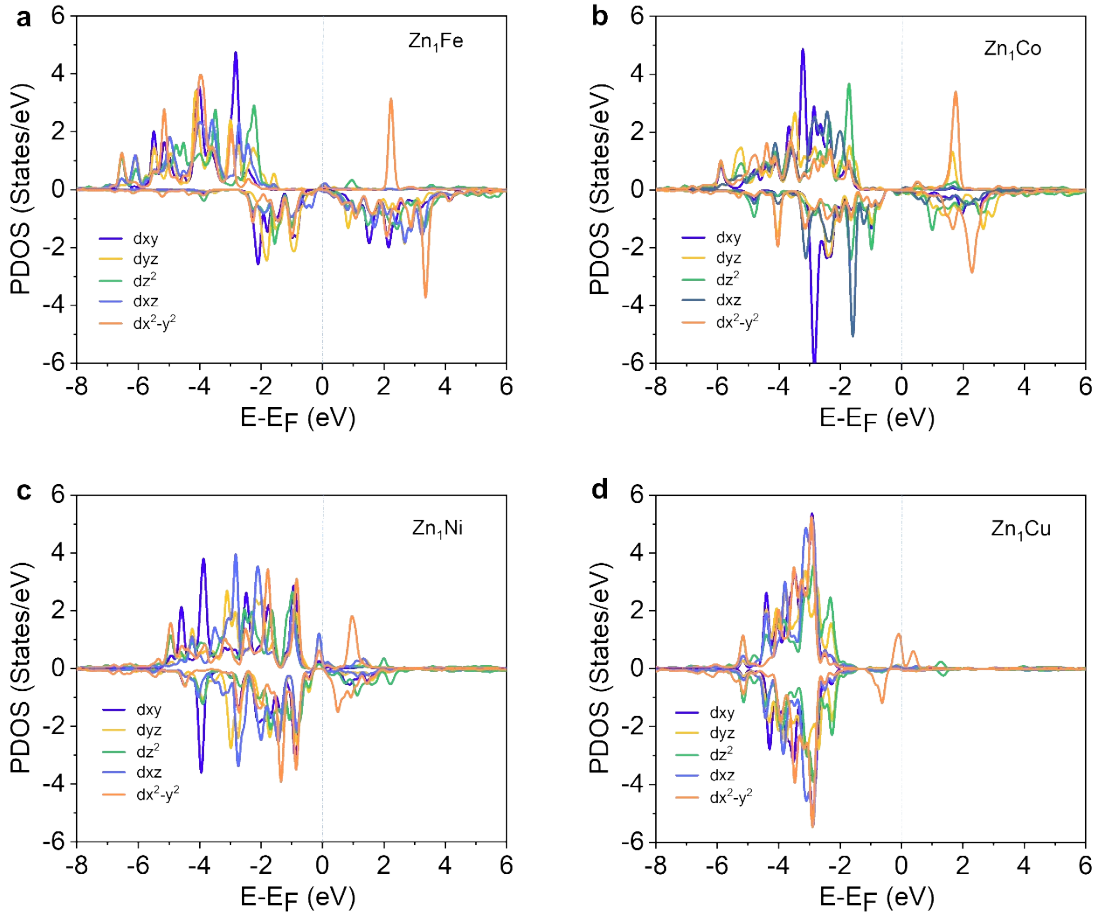

Fig. S13. The PDOS of different ACCs.

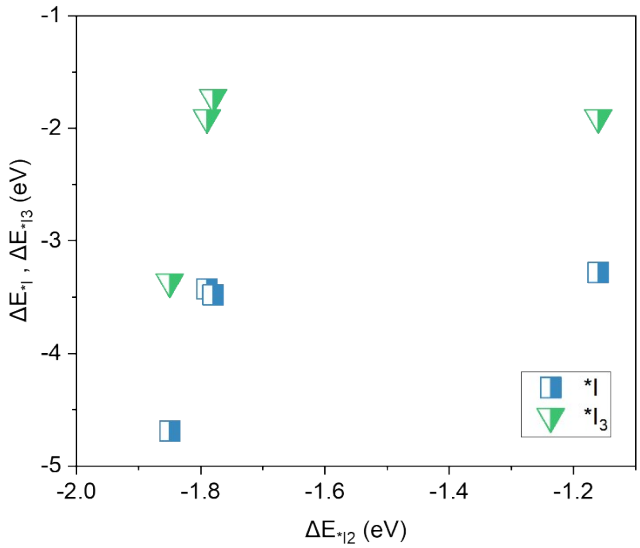

Fig. S14. The adsorption energy of three iodine intermediates (*I_2, *I_3, and *I) in Zn_1M ACCs (M=Fe, Co, Ni, Cu).

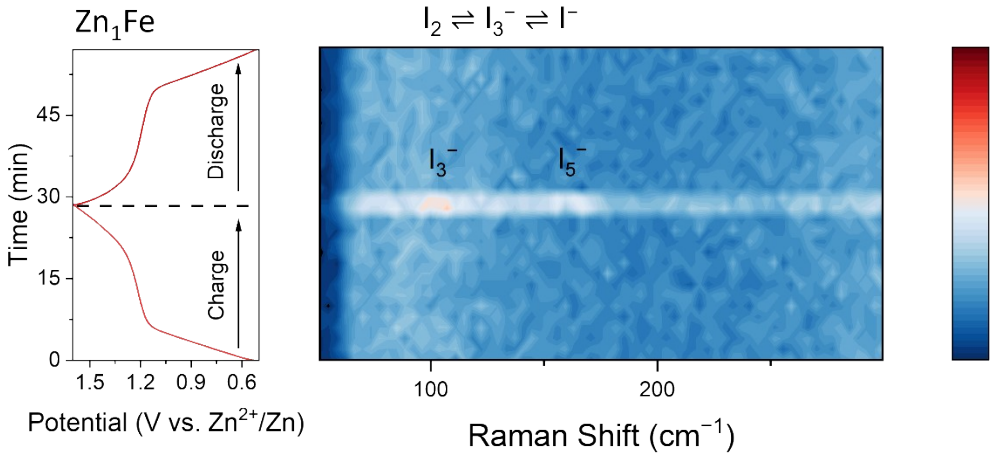

Fig. S15. *In situ* Raman spectra during cyclic charging-discharging cycles for the Zn_1Fe electrode.

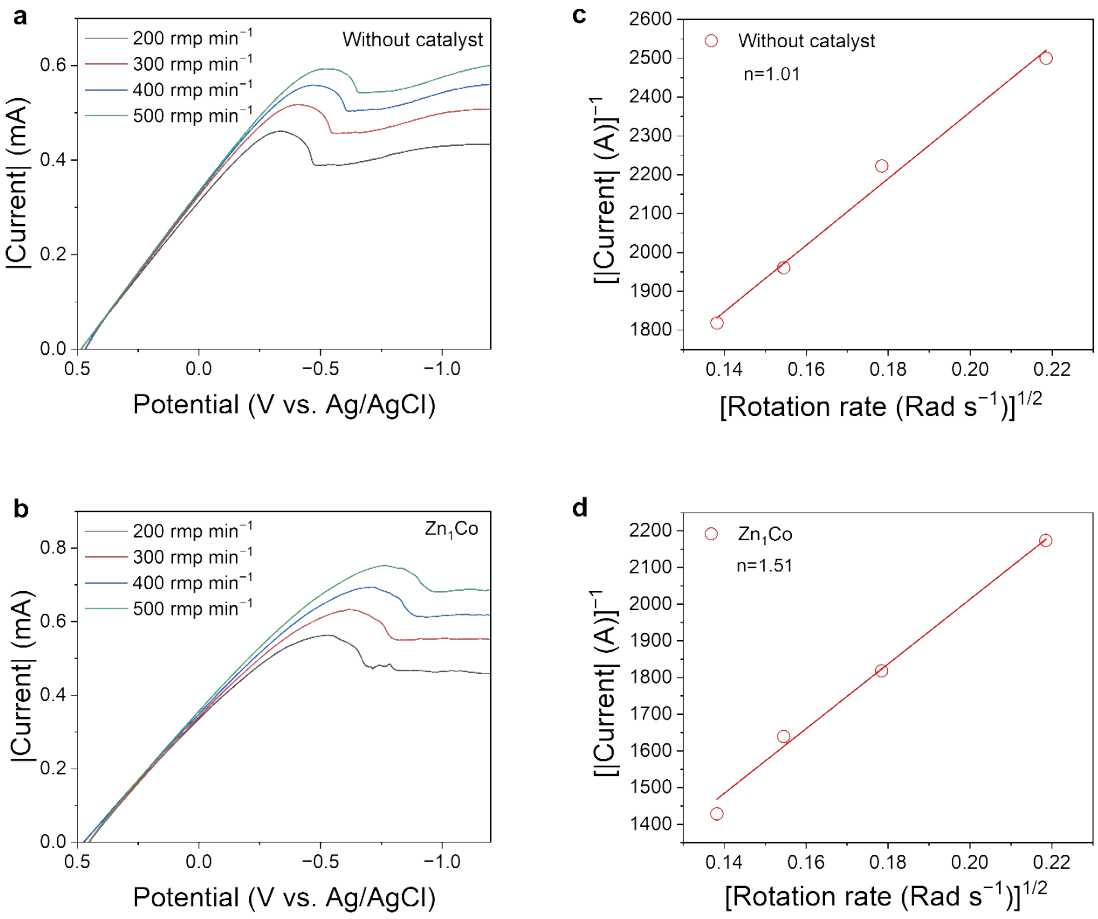

Fig. S16. Electrochemical characterization of catalysts via RDE. (a–b) LSV curves of (a) blank sample and (b) Zn_1Co ACCs for the iodine reduction reaction with different rotation rates in a solution containing 0.5 mM of I_2 and 0.5 mM of I^-. (c–d) Koutecky-Levich plots derived from LSV data at −0.5 V vs. Ag/AgCl, revealing electron transfer numbers of (c) n = 1.01 for the blank sample and (d) n = 1.51 for Zn_1Co ACCs.

Koutecky–Levich analysis via rotating disk electrode (RDE) and linear sweep voltammetry (LSV) at varying rotation rates (200–500 rpm) shows a greater increase in current density for the Zn_1Co/I_2 electrode compared to the catalyst-free system, indicating accelerated charge-transfer kinetics (Fig. S16). The electron transfer number (n) is 1.01 for the blank and 1.51 for

Zn_1Co/I_2, both below the theoretical value of 2, suggesting incomplete polyiodide reduction without catalysis and enhanced multi-electron transfer with Zn_1Co/I_2.

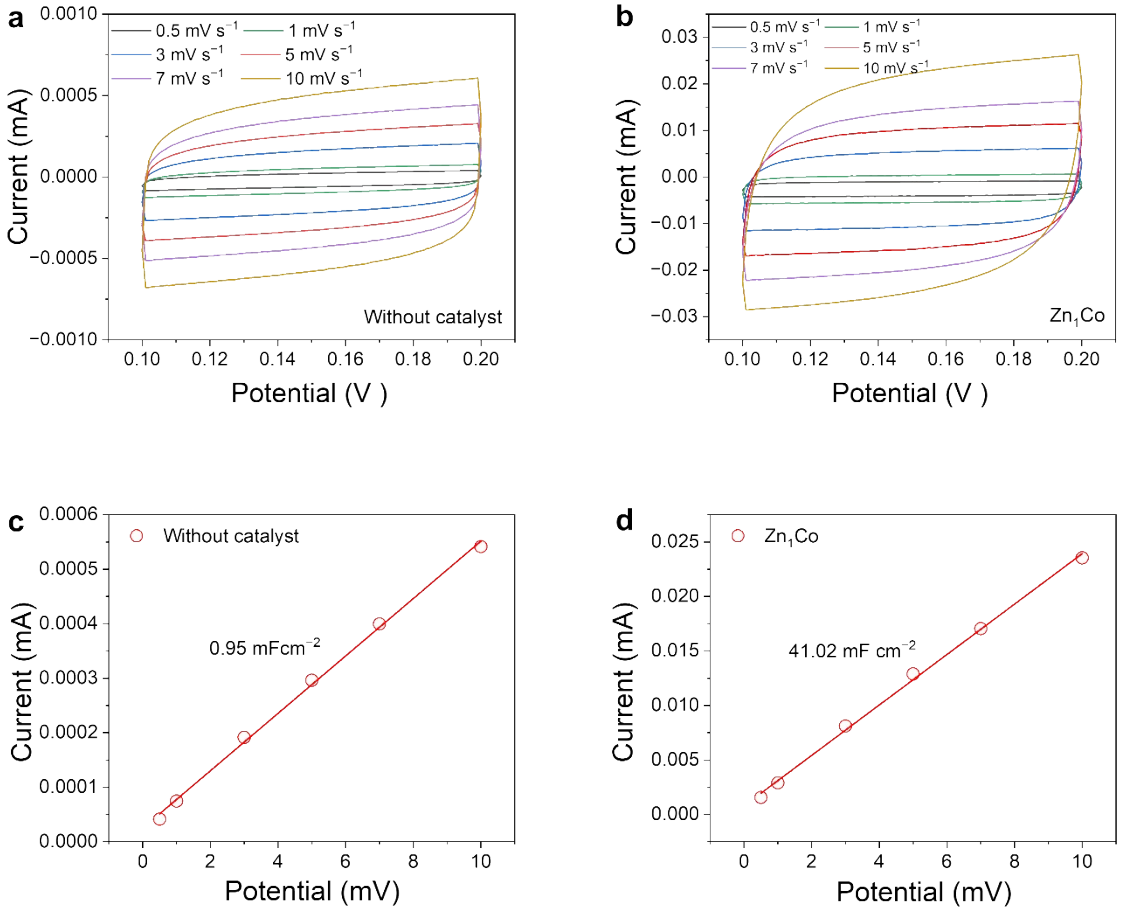

Fig. S17. ECSA characterization. (a–b) CV curves of I_2 cathode (a) without catalyst and (b) with Co_1Zn ACCs at different scan rates (0.5–10 mV s^{-1}) in 2 M $ZnSO_4$. (c–d) Linear regression analysis of capacitive current vs. scan rate for (c) blank sample and (d) Co_1Zn ACCs.

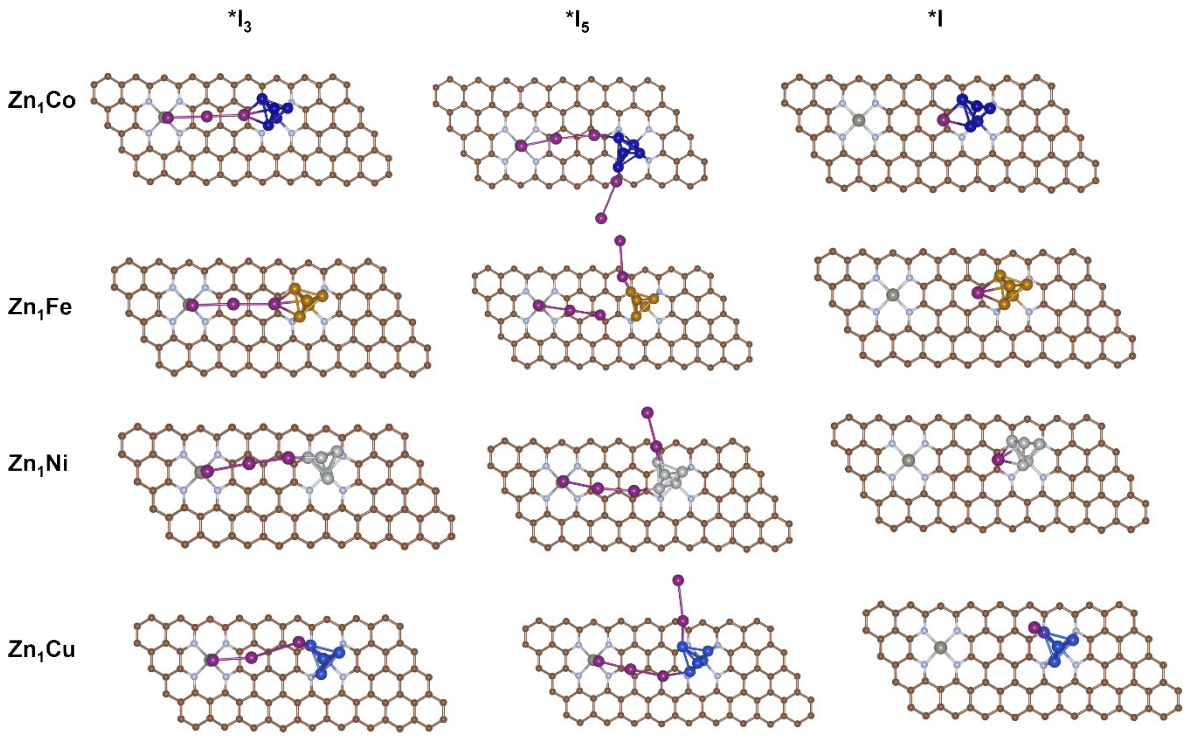

Fig. S18. The optimized atomic structures of *I, *I_3, and *I_5 adsorbed on different Zn_1M ACCs. Brown, dark grey, silver, light grey, blue, dark blue, golden yellow, and purple represent atoms C, Zn, N, Ni, Cu, Co, Fe, and I, respectively.

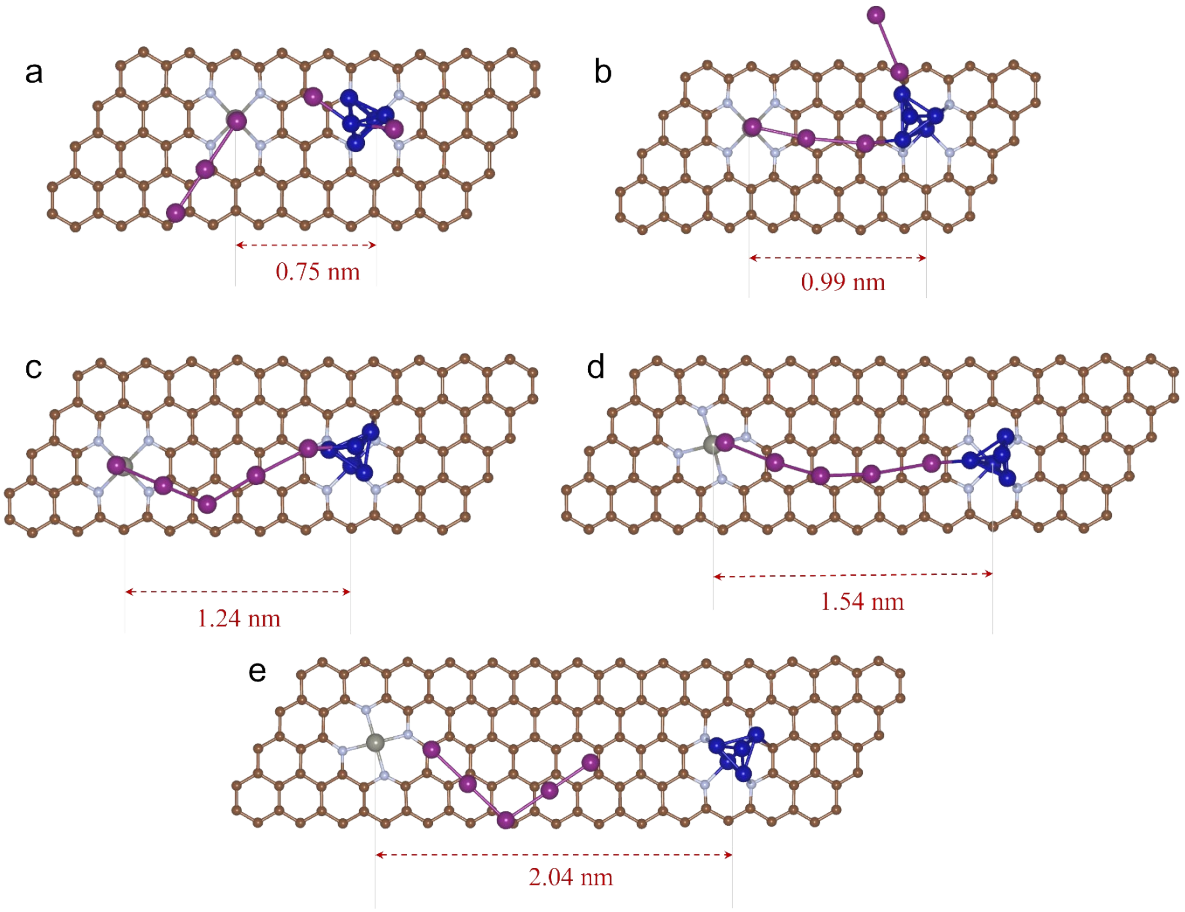

Fig. S19. The optimized atomic structures of $*I_5$ adsorbed on Zn_1Co ACCs with different distances. Brown, dark grey, silver, dark blue, and purple represent atoms C, Zn, N, Co and I, respectively.

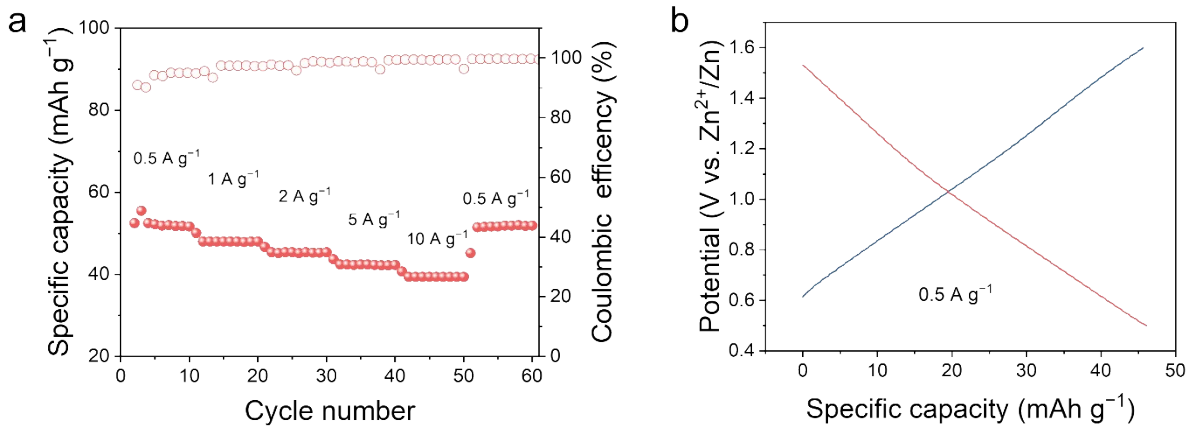

Fig. S20. Electrochemical performance of the porous carbon host. (a) Rate capability and corresponding Coulombic efficiency at various current densities. (b) Galvanostatic charge-discharge voltage profiles at a current density of 0.5 A g^{-1}.

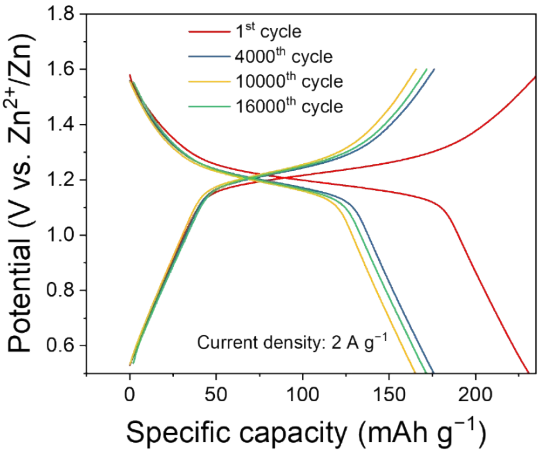

Fig. S21. Charge–discharge profiles for Zn_1Co/I_2 electrode at the current density of 2 A g^{-1}.

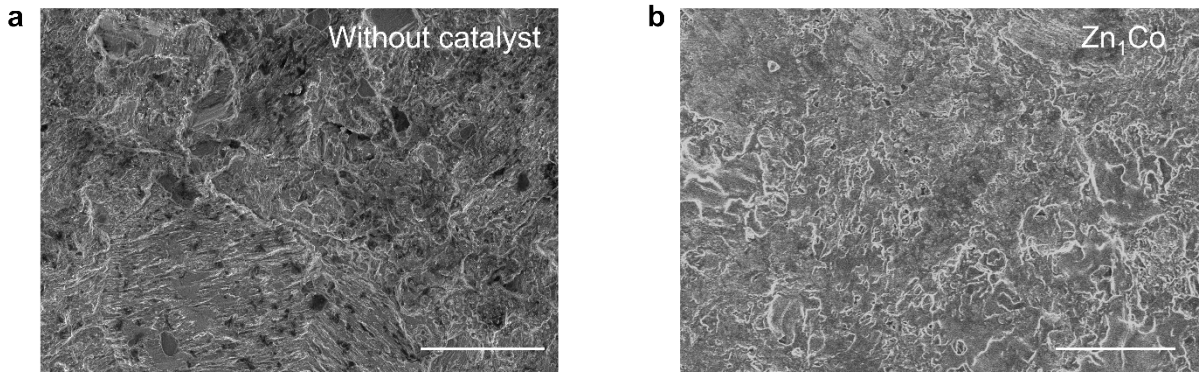

Fig. S22. SEM images of zinc anode without catalysts and with Zn_1Co ACCs after cycling, scale bar: 10 μm.

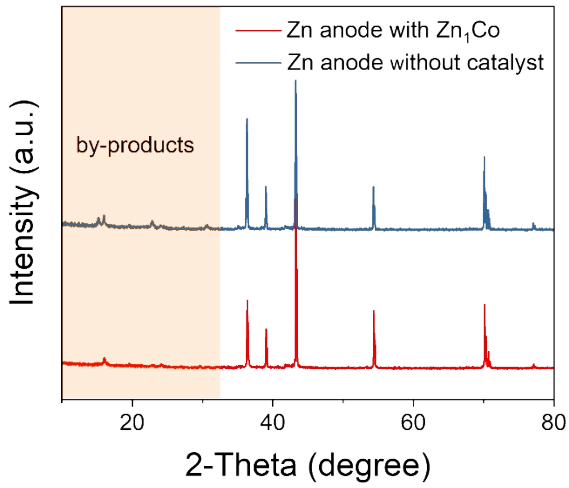

Fig. S23. XRD images of zinc anode after cycling.

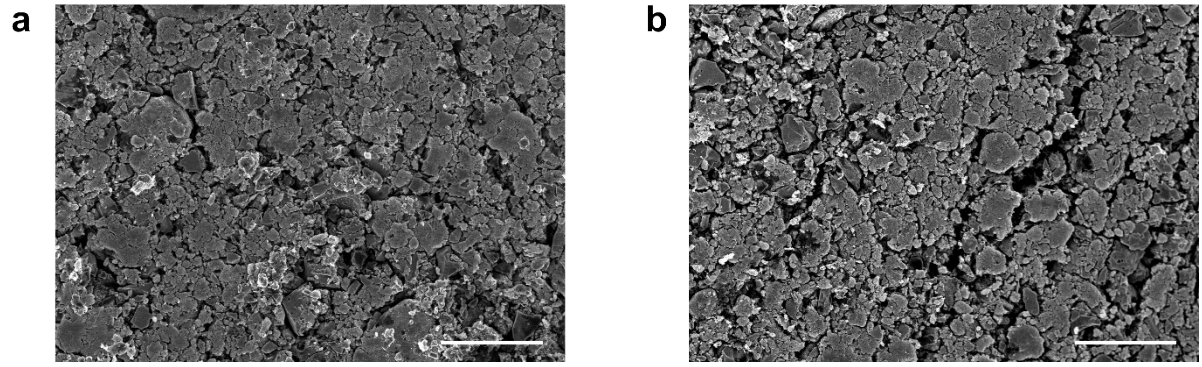

Fig. S24. SEM images of the Zn_1Co/I_2 cathode (a) before cycling and (b) after 100 cycles at 2 A g^{-1}, scale bar: 100 μm.

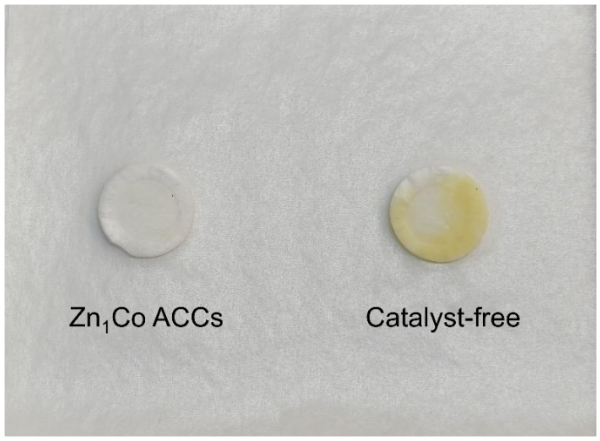

Fig. S25. Optical images of separators disassembled from cells with Zn_1Co ACCs/I_2 and catalyst-free electrodes.

Table S1. Fitted R_{ct} values for Zn-I_2 cells with ACCs/I_2 electrodes under different temperatures.

	Temperature	25°C	30°C	35°C	40°C
Zn_1Fe	R_{ct} (Ω)	39.83	31.23	28.47	26.48
	Error(%)	4.78	5.54	4.13	4.34
Zn_1Co	R_{ct} (Ω)	92.79	74.33	58.31	53.26
	Error(%)	2.49	3.65	5.64	3.39
Zn_1Ni	R_{ct} (Ω)	47.24	42.35	39.47	35.76
	Error(%)	3.12	3.55	2.72	5.87
Zn_1Cu	R_{ct} (Ω)	60.13	51.56	42.45	38.26
	Error(%)	4.81	3.55	4.64	5.43

Table S2. The d band center of M cluster in different Zn_1M ACCs (M=Fe, Co, Ni, Cu).

Materials	Spin-up (eV)	Spin-down (eV)
Zn_1Fe	-3.71	0.69
Zn_1Co	-2.78	-0.82
Zn_1Ni	-2.43	-1.73
Zn_1Cu	-3.24	-3.28

Table S3. The unpair electron number of M cluster in different Zn_1M ACCs (M=Fe, Co, Ni, Cu).

Materials	Unpair electron number (e)
Zn_1Fe	1.34
Zn_1Co	0.54
Zn_1Ni	0.13
Zn_1Cu	0.04

Table S4. The adsorption energy of three iodine intermediates ($*I_2$, $*I_3$, and *I) in Zn_1M ACCs (M=Fe, Co, Ni, Cu).

Materials	ΔE_{*I2}	ΔE_{*I3}	ΔE_{*I}
Zn_1Fe	-1.85	-4.69	-3.365
Zn_1Co	-1.79	-3.43	-1.905
Zn_1Ni	-1.7	-3.48	-1.725
Zn_1Cu	-1.16	-3.28	-1.905

Table S5. The thermodynamic energy barriers for the conversion of I_3^- to I^- in different Zn_1M ACCs (M=Fe, Co, Ni, Cu).

Materials	ΔG (eV)
Zn_1Fe	-0.04
Zn_1Co	-0.13
Zn_1Ni	-0.11
Zn_1Cu	0.06

References

1. G. Kresse and J. Furthmüller, *Phys. Rev. B* 1996, **54**, 11169-11186.
2. P. E. Blöchl, *Phys. Rev. B* 1994, **50**, 17953-17979.
3. G. Kresse and J. Hafner, *Phys. Rev. B* 1993, **47**, 558-561.
4. J. P. Perdew, K. Burke and M. Ernzerhof, *Phys. Rev. Lett.* , 1996, **77**, 3865-3868.
5. G. Kresse and J. Furthmüller, *Phys. Rev. B* 1996, **6**, 15-50.